Constraining ventilation during deepwater formation using deep ocean measurements of the dissolved gas ratios $^{40}Ar/^{36}Ar$, N_2/Ar, and Kr/Ar

David Nicholson,[1] Steven Emerson,[2] Nicolas Caillon,[3] Jean Jouzel,[3] and Roberta C. Hamme[4]

[1]   The concentration of inert gases and their isotopes in the deep ocean are useful as tracers of air-sea gas exchange during deepwater formation. $\Delta Kr/Ar$, $\Delta N_2/Ar$, and $\delta^{40}Ar$ were measured in deep profiles of samples collected in the northwest Pacific, subtropical North Pacific and tropical Atlantic oceans. For the ocean below 2000 m, we determined a mean $\Delta Kr/Ar$ composition of $-0.96\% \pm 0.16\%$, a mean $\Delta N_2/Ar$ of $1.29\% \pm 0.21\%$ relative to equilibrium saturation, and for $\delta^{40}Ar$ a value of $1.188\text{‰} \pm 0.055\text{‰}$ relative to air. These data are used to constrain high-latitude ventilation processes in the framework of three-box and seven-box ocean models. For the three-box model tracer data, we constrain the appropriate surface area of the high-latitude region in both models to be 3.6% (+2.5%, −1.7%) of ocean surface area and the bubble air injection rate to be 22.7 (+8.8, −7.3) mol air m^{-2} yr^{-1}. Results for the seven-box model were similar, with a high-latitude area of 3.3% (+2.2%, −1.3%). Our results provide geochemical support for suggestions that the effective area of high-latitude ventilation is much smaller than the region of elevated preformed nutrients and demonstrate that noble gases strongly constrain the ocean solubility pump. Reducing high-latitude surface area weakens the CO_2 solubility pump in the box models and limits communication between the atmosphere and deep ocean. These tracers should be useful constraints on high-latitude ventilation and the strength of the solubility pump in more complex ocean general circulation models.

1.   Introduction

[2]   Cycling of carbon in the marine system is controlled by complex interactions between physical and biological processes. Untangling the relative contributions of physics and biology is a great challenge. N_2 and the noble gases (He, Ne, Ar, Kr, and Xe) are inert gases that can be used as tracers of the physical processes that drive air-sea gas exchange (because of its great abundance, N_2 behaves largely conservatively through most of the ocean, despite small deviations due to biological cycling of nitrogen, particularly in oxygen minimum zones). In this paper we present new measurements of N_2/Ar, Kr/Ar, and $\delta^{40}Ar$ and incorporate them into ocean box models to constrain high-latitude ventilation processes. Gas exchange at high latitudes is critical to the carbon cycle because these regions feed the vast ocean interior. Using inert gases can lead us to a better understanding of the physical processes that cycle all gases in the ocean.

1.1.   Ocean Controls on Atmospheric pCO2

[3]   Glacial/interglacial cycles in the pCO2 of the atmosphere of ~80–90 ppm have been well recorded in ice cores [*Luthi et al.*, 2008; *Petit et al.*, 1999] and strongly correlate with temperature and ice volume. While the relationship between pCO2 and climate has been well documented, a satisfactory mechanism that explains the cycles of pCO2 remains elusive. Early box model studies suggested uptake of unutilized high-latitude nutrients during glacial times as a means to draw down pCO2 [*Knox and McElroy*, 1984; *Sarmiento and Toggweiler*, 1984, hereafter ST84; *Siegenthaler and Wenk*, 1984]. These early box model studies introduced the idea of high-latitude sensitivity of the marine carbon cycle. This led to further hypotheses such as iron limitation as a control on the high-latitude biological pump [*Martin et al.*, 1990]. Other theories, such as southern ocean sea ice hypotheses, [*Gildor and Tziperman*, 2001; *Sigman and*

[1]Department of Marine Chemistry and Geochemistry, Woods Hole Oceanographic Institution, Woods Hole, Massachusetts, USA.
[2]School of Oceanography, University of Washington, Seattle, Washington, USA.
[3]Laboratoire des Sciences du Climat et de l'Environnement, IPSL, CEA, CNRS, UVSQ, Gif-sur Yvette, France.
[4]School of Earth and Ocean Sciences, University of Victoria, Victoria, British Columbia, Canada.

Boyle, 2000; *Stephens and Keeling*, 2000], polar ocean stratification [*Sigman et al.*, 2004], and biogeochemical divides [*Marinov et al.*, 2006; *Toggweiler*, 1999] also rely on atmospheric pCO_2 being controlled primarily by high-latitude processes.

[4] General circulation models (GCMs) and box models do not always agree on the effectiveness of these hypotheses in modulating atmospheric pCO_2. In general, GCM studies place a higher emphasis on the importance of low-latitude nutrient uptake, while box model approaches favor high-latitude triggers [*Archer et al.*, 2003]. This may be due to the difference in how deep water is formed in GCMs versus box models. Box models tend to have large high-latitude outcrops, allowing for a high degree of communication between the deep ocean and the atmosphere [*Toggweiler et al.*, 2003a, 2003b]. GCMs, on the other hand, have a less efficient solubility pump, creating deep water that is further from equilibrium than do box models [*Archer et al.*, 2000].

[5] One way to quantify the efficiency of the biological soft tissue pump is in terms of preformed nutrient concentration [*Broeker and Peng*, 1982; *Ito and Follows*, 2005]. Higher preformed nutrients are diagnostic of a weaker biological pump and higher atmospheric pCO_2. *Ito and Follows* [2005] argue that it is difficult to lower preformed nutrients because deep water forms in convective columns with very limited areal extent (i.e., a small surface area for deepwater formation regions). The convective upwelling of nutrient-rich water precludes a significant drawdown of nutrients in formation regions.

[6] *Toggweiler et al.* [2003a, 2003b, hereafter T03], compared how box models and GCMs represent the solubility and biological ocean carbon pumps. The authors argue that the unrealistic solubility pump in box models is simply an artifact of too much surface area in the high-latitude surface box and that GCMs unduly inhibit gas exchange at high latitudes. The real ocean, argues T03, lies somewhere between the states represented by GCMs and traditional box models.

1.2. Inert Gases and Their Isotopes as Tracers

[7] To model how ocean physics and biology influence atmospheric pCO_2, it is essential to better understand the mechanisms of gas exchange during deepwater formation. We use new measurements of $^{40}Ar/^{36}Ar$, Kr/Ar, and N_2/Ar ratios in the deep sea to constrain air-sea gas transfer during deepwater formation. Each of these gases has well-known and constant atmospheric mixing ratio and isotopic composition, and to a first approximation, their seawater concentrations are in chemical equilibrium with the overlying atmosphere. During deepwater formation, small deviations from saturation of a few percent are caused by processes such as heating/cooling of water, injection of air bubbles under rough surface conditions, and atmospheric pressure variations [*Hamme and Emerson*, 2002; *Hamme and Severinghaus*, 2007]. The air-sea heat flux and associated cooling drives the gases toward undersaturation, while the injection of bubbles increases the concentration. Since saturation states of ocean samples are referenced to one atmosphere, climatologically low atmospheric pressure in high-latitude regions of deepwater formation further contributes to undersaturation. As high-latitude water cools, it subducts before it can fully equilibrate with the atmosphere.

Once leaving the surface, a parcel of water carries to the deep ocean the saturation signature acquired during formation. Using several gases, we can explain how the balance of processes at the air-sea interface determines gas concentrations during deepwater formation.

[8] Each gas has a unique sensitivity to the processes contributing to the departure from saturation [see *Hamme and Severinghaus*, 2007]. As a general rule, lighter gases are less soluble than heavier gases. Although the solubility of all of the gases decreases with increasing water temperature, the lighter gases generally have a solubility that is less temperature dependent than do heavier gases. For this reason, heavier gases are more sensitive to cooling. The lighter (less soluble) gases are most sensitive to bubble processes because they are much more abundant in the atmosphere relative to seawater. Here we focus our attention on gas and isotope ratios as tracers because this removes the sensitivity to atmospheric pressure. Response of the gas ratios to the mechanisms causing departure from saturation depends on a combination of the physical processes of both gases. N_2/Ar is particularly sensitive to bubble injection fluxes, because nitrogen is about half as soluble as argon, but both gases have very similar temperature-solubility functions. Kr/Ar and $\delta^{40}Ar$ are both more sensitive to cooling during deepwater formation.

2. Analytical Methods

[9] We present the data in terms of saturation anomalies for the gases and delta values for the isotopes. Before further discussion, we introduce some notation that will be used through this paper. The degree that the dissolved concentration of a gas, $[C]$, varies from the concentration that would be in equilibrium with the atmosphere (at 1 atm), $[C]_{sat}$, is normalized to the atmospheric equilibrium concentration to give the saturation anomaly ΔC.

$$\Delta C = 100 \times \left(\frac{[C]}{[C]_{sat}} - 1 \right). \tag{1}$$

Negative values of ΔC indicate undersaturation, and positive values indicate supersaturation, relative to atmospheric equilibrium. A similar notation is used for the ratio of two gases, C_1 and C_2, where

$$\Delta C_1/C_2 = 100 \times \left[\frac{([C_1]/[C_2])}{([C_1]_{sat}/[C_2]_{sat})} - 1 \right]. \tag{2}$$

For the isotopes $^{40}Ar/^{36}Ar$ we use the standard stable isotope notation in which the ratio is reported in per mil units relative to a standard, which here is the atmospheric isotope ratio, $(^{40}Ar/^{36}Ar)_{air}$:

$$\delta^{40}Ar = 1000* \left[\frac{\left(^{40}Ar/^{36}Ar \right)}{\left(^{40}Ar/^{36}Ar \right)_{air}} - 1 \right]. \tag{3}$$

[10] Samples for dissolved gases were collected from four locations: the eastern tropical Atlantic (10°N, 27°W), northwest Pacific (47°N, 167°E), subtropical North Pacific Gyre (26°N, 152°W), and the Hawaii Ocean Time-series (22°45′N, 158°W) (Figure 1). These locations are hereafter referred to
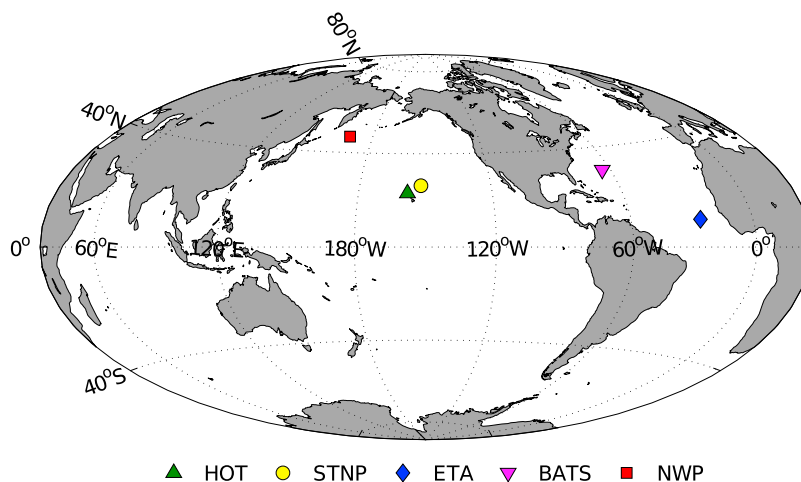
Figure 1. N_2/Ar, Kr/Ar, and $\delta^{40}Ar$ sampling locations. Samples were collected from October 2007 through September 2008 in evacuated glass flasks and stored for analysis. Deep profiles were collected from the eastern tropical Atlantic (blue diamond; 10°N, 27°W), northwest Pacific (red square; 47°N, 167°E), and subtropical North Pacific Gyre (yellow circle; 26°N, 152°W). Samples from the Hawaii Ocean Time-series (HOT) (green triangle; 22.75°N, 158°W) were collected from 2001 to 2003. Previously published N_2/Ar measurements were from samples collected at HOT, and the Bermuda Atlantic Time Series (magenta inverted triangle) [Hamme and Emerson, 2002].

as the ETA, NWP, STNP, and HOT, respectively. The first measurements of the argon isotope ratios were obtained from HOT in 2002–2003 and were measured by Nicolas Caillon and Roberta Hamme in the laboratories of Jean Jouzel at Commissariat à l'Energie Atomique (CEA) Saclay, France and Jeff Severinghaus at Scripps Institute of Oceanography, University of California, San Diego. The rest of the samples were collected in 2007 and 2008 and measured in the mass spectrometry laboratories at the University of Washington.

[11] All samples were collected in duplicate or triplicate in ~160 mL evacuated glass flasks, fitted with Louwers Hapert double O-ring stopcocks, by filling flasks half to three-quarters full with seawater from Niskin bottles, using procedures to avoid any atmospheric contamination [Emerson et al., 1999].

[12] Gases in sample flasks were extracted in the lab on a vacuum line to prepare them for analysis on the mass spectrometer. Extraction methods were similar to previous studies that have measured $\delta^{40}Ar$ and Kr/Ar in ice cores [Severinghaus et al., 2003] and Kr/Ar in seawater [Hamme and Severinghaus, 2007]. During extraction the first step is to remove water vapor and CO_2 in traps cooled with a liquid nitrogen and ethanol slurry (~ −90 K). N_2 and O_2 gases are then removed by exposing the sample to a Zr/Al alloy getter, material (SAES Getters Group) heated to 900°C in a quartz oven, leaving only the noble gases. Ultra high purity (UHP) nitrogen is added to the noble gas sample in a 35:1 molar ratio to serve as a carrier gas during mass spectrometry. The sample is then captured in a stainless steel sample tube cooled with liquid helium.

[13] The gas and isotope ratios of each sample were measured against a working standard that was created from UHP nitrogen, argon and krypton gases in ratios that are approximately equal to observed deep ocean $N_2:Ar:Kr$ molar ratios (about $35:1:2 \times 10^{-4}$). To calculate the precise gas ratios of the working standard, it was routinely measured against air.

The molecular fractional composition of gases in air is well documented [Glueckauf, 1951] and served as the ultimate standard for our measurements. Prior to measurement, the reference air sample was extracted on the vacuum line using the exact same procedure used for the seawater gas samples. We assumed any small gas or isotope fractionation occurring during extraction should affect both seawater and reference air samples and cancels to a first order. The working standard was measured against air once a day, before samples were run.

[14] Samples were measured on a Finnigan 253 isotope ratio mass spectrometer following the processes described by Severinghaus et al. [2003]. We adopted several methods used by Severinghaus et al. [2003] to improve the precision of the method. The measured $^{40}Ar/^{36}Ar$ is slightly sensitive to pressure imbalances between the inlet sides. Pressure in the bellows is manually balanced to improve control over the voltage on each inlet side. A calibration curve was created to correct for small variations in the N_2/Ar ratio. The slope was $(1.63 \times 10^{-3}$ (‰ $\delta^{40}Ar$)/(‰ $N_2:Ar$)) which was slightly greater than the slope of 1.0×10^{-3} observed by Severinghaus et al. [2003]. The magnitude of the correction applied to the seawater samples ranged up to about 0.01‰.

[15] After making the corrections outlined above, the mean $\delta^{40}Ar$ value of the working standard relative to reference air samples was −10.701‰ with a standard deviation of 0.019‰ and a standard error of the mean (s.e.) for the ten measurements was 0.006‰ (s.e. = $0.019/10^{0.5}$ = 0.006‰) (Our notation for this is $\delta^{40}Ar$ = −10.701‰ ± 0.019‰ (s.e. = 0.006‰, n = 10)). The $\delta(Kr/Ar)$ of the working standard relative to reference air was −369.14‰ ± 0.35‰ (s.e. = 0.11‰, n = 9). For both $\delta^{40}Ar$ and Kr/Ar, there was no statistically significant trend in reference air versus working standard values over the duration of the measurements.

[16] For the NWP, replicate samples were also collected and measured for the dissolved N_2/Ar gas ratios (Figure 2c).
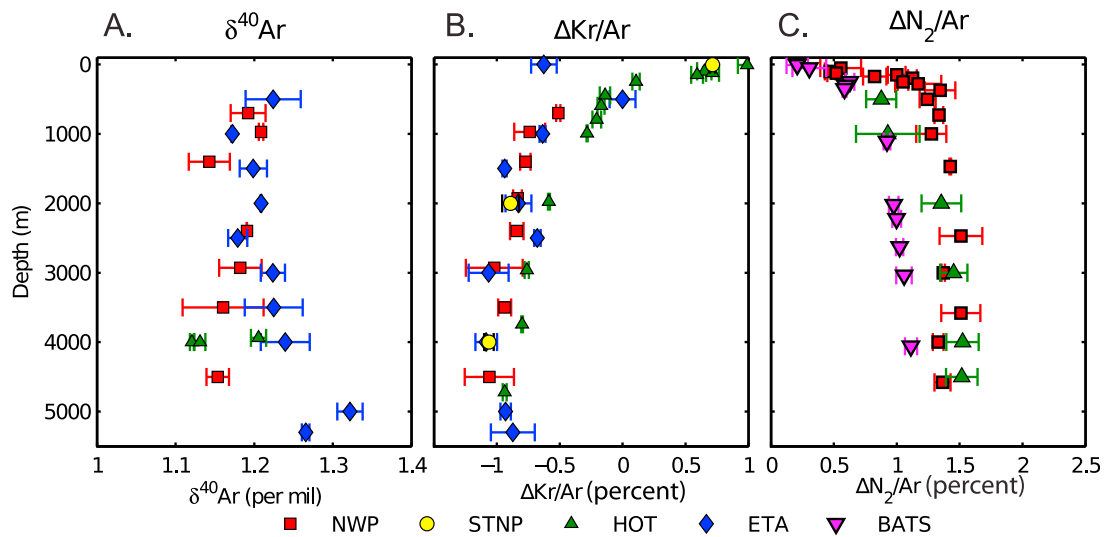
Figure 2. Depth profiles are shown for (a) $\delta^{40}Ar$, (b) $\Delta Kr/Ar$, and (c) $\Delta N_2/Ar$. Eastern tropical Atlantic (ETA) in blue diamonds, northwest Pacific (NWP) in red squares, subtropical North Pacific (STNP) in yellow circles, Hawaii Ocean Time-series (HOT) in green triangles, and the Bermuda Atlantic Time Series in magenta inverted triangles. HOT $\Delta Kr/Ar$ data are reproduced from *Hamme and Severinghaus* [2007]. Error bars are one standard deviation of duplicate pairs.

These samples were collected in the same manner as described above. An isotope spike of ^{36}Ar was added to each sample to calculate absolute gas concentrations via isotope dilution as well as gas ratios. Samples were processed using a simpler method than for $\delta^{40}Ar$ and Kr/Ar, i.e., without a getter oven removal of N_2 and O_2 as described by *Hamme and Emerson* [2006].

3. Results

[17] A total of 27 sets of duplicate samples were collected for $\delta^{40}Ar$ and $\Delta Kr/Ar$ at the four sampling sites (Table A1). Three of the 54 samples were lost during the sampling and preprocessing phase of analysis. Two additional pairs were rejected because of large discrepancies between duplicates (when the standard deviation of a pair exceeded triple the average standard deviation of duplicates, both were discarded). For $\Delta N_2/Ar$, 20 sets of duplicate pairs were collected in the NWP.

[18] On average, the standard deviation of duplicate pairs for $\delta^{40}Ar$ was 0.017‰, 0.027‰, and 0.010‰ for the ETA, NWP, and HOT samples, respectively. The mean of the standard deviations of all duplicates was 0.020‰. The $\delta^{40}Ar$ at ETA generally increased with depth below 1000 m, while a trend in NWP with depth was not apparent (Figure 2a). To determine a mean composition of the deep ocean, we take the mean of samples from 2000 m and below, then average the result from our three locations (two from the Pacific and one from the Atlantic). The error estimate is the standard deviation of all samples collected below 2000 m for each gas ratio. The mean, standard deviation, and standard error of $\delta^{40}Ar$ of deep samples for ETA, NWP, and HOT was 1.24‰ ± 0.046‰ (s.e. = 0.015‰, $n = 10$), 1.172‰ ± 0.028‰ (s.e. = 0.010‰, $n = 8$), and 1.155‰ ± 0.042‰ (s.e. = 0.015‰, $n = 8$), respectively. The mean of the $\delta^{40}Ar$ of the three deep regions was 1.188‰ ± 0.055‰ ($n = 28$).

[19] For $\Delta Kr/Ar$, the mean standard deviations were 0.83‰, 0.93‰, and 1.10‰ for ETA, NWP, and STNP samples, respectively. For all duplicates, the average standard deviation was 0.092%. All locations showed a relatively consistent negative $\Delta Kr/Ar$ values at and below 2000 m (Figure 2b). Both cooling and bubble injection can make $\Delta Kr/Ar$ negative, and observed values are likely due to a combination of the two processes. In the thermocline and above, two processes that cause a positive $\Delta Kr/Ar$ signal, diapycnal mixing and heating, become more important, and $\Delta Kr/Ar$ values trend toward more positive values. Mixing increases $\Delta Kr/Ar$ because of the greater nonlinearity in the temperature dependence of Kr compared to Ar [*Ito and Deutsch*, 2006]. For $\Delta Kr/Ar$, the mean and standard error of deep samples was −0.91% ± 0.16% (s.e. = 0.048%, $n = 12$), −0.94% ± 0.15% (s.e. = 0.045%, $n = 10$) and −1.03% ± 0.18% (s.e. = 0.055%, $n = 4$) for ETA, NWP, and STNP, respectively. For the average of the deep locations, $\Delta Kr/Ar$ was −0.96% ± 0.16% ($n = 26$). A summary of these results is presented in Table 1.

Table 1. Summary and Statistics for Measurements of D(Kr/Ar) and $\delta^{40}Ar$[a]

	$\Delta Kr/Ar$ (%)	$\delta^{40}Ar$ (‰)
	Replicates	
ETA	0.083	0.017
NWP	0.093	0.027
STNP/HOT	0.110	0.010
All pairs	0.092	0.020
	Pooled Deep Samples	
ETA	−0.910 (0.163)	1.215 (0.046)
NWP	−0.939 (0.147)	1.172 (0.028)
STNP/HOT	−1.028 (0.182)	1.155 (0.042)
All deep	−0.959 (0.162)	1.188 (0.055)

[a]Standard deviations given for replicates. Means with standard deviations given in parentheses given for pooled deep samples.

Table 2a. Physical Properties of Gases at 2.5°C

Gas	Solubility β_C[a] (mol kg^{-1})	Relative Solubility β_C/β_{Ar}	Solubility T Dependence $\frac{d\beta_c/dT}{\beta_c}$ (%/°C)	Schmidt Number Sc_C[b]	Transfer Coefficient k_C[c] (m/d)	Relative Transfer Coefficient k_C/k_{Ar}
Ne	4.323×10^{-4}	0.439	−0.99	685.6	5.05	1.071
N$_2$	7.532×10^{-4}	0.439	−2.28	1232.2	3.98	1.071
Ar	1.715×10^{-3}	–	−2.46	1059.3	3.72	–
^{36}Ar	1.713×10^{-3}	0.9988	−2.46	1070.0	3.73	1.005
Kr	3.425×10^{-3}	1.998	−3.07	1793.6	3.17	0.852
CO$_2$	5.72×10^{-2}	333.5	−3.77	1781.0	3	0.807

[a]Solubility data are from *Hamme and Emerson* [2004b] for Ne, N$_2$ and Ar, from *Weiss and Kyser* [1978] for Kr, and from *Weiss* [1974] and *Zeebe and Wolfe-Gladrow* [2001] for CO$_2$.

[b]Schmidt numbers for Ne, N$_2$, Ar, and Kr were calculated from gas diffusivities [*Jähne et al.*, 1987a]. Schmidt number for CO$_2$ is from the temperature-dependent parameterization of *Wanninkhof* [1992].

[c]The mass transfer coefficient for CO$_2$ is prescribed in the box model, while the transfer coefficient for the other gases is calculated on the basis of Schmidt number dependence.

[20] The average standard deviation of $\Delta N_2/Ar$ for all duplicate pairs was 0.09%. For pooled NWP deep samples, $\Delta N_2/Ar$ was 1.44% ± 0.11% ($n = 22$). To estimate $\Delta N_2/Ar$ in other regions of the deep ocean comparable to the STNP and ETA, we used previously published $\Delta N_2/Ar$ measurements [*Hamme and Emerson*, 2002] (Figure 2c). Deep ocean mean values were calculated for each region. In the STNP, on the basis of measurements at HOT, deep $\Delta N_2/Ar$ was 1.43% ± 0.11% ($n = 50$), while in the Atlantic, $\Delta N_2/Ar$ was 1.03% ± 0.08% ($n = 29$) based on observations at the Bermuda Atlantic Time Series (BATS) (30°40′N, 64°10′W). We calculate a mean deep ocean $\Delta N_2/Ar$ value that is comparable to those for $\Delta Kr/Ar$ and $\delta^{40}Ar$ by averaging the values for the three regions above to get a value of $\Delta N_2/Ar$ = 1.29% ± 0.21%.

[21] For all profiles, $\Delta N_2/Ar$ is close to equilibrium at the surface and increases with depth. $\Delta N_2/Ar$ is primarily influenced by bubble processes, so this trend is likely due to the increasing role of bubble fluxes in the high-latitude regions that ventilate the deep ocean. Higher Southern Ocean bubble fluxes likely contribute to the observed higher $\Delta N_2/Ar$ in the Pacific relative to the Atlantic, but the possibility of a role for ice process [*Hohmann et al.*, 2002; *Rodehacke et al.*, 2007; *Well and Roether*, 2003] and denitrification in adding N$_2$ should not be discounted.

4. Discussion

4.1. Gas Solubility and Molecular Diffusion

[22] The process of atmosphere-ocean gas exchange depends on the solubility and molecular diffusion coefficients of gases. Values for the gases and isotopes we use here are presented in Tables 2a and 2b. All of the values are from the literature except for the chemical equilibrium and kinetic fractionation factors for the argon isotopes. Kinetic fractionation factors were measured in our laboratory and are presently unpublished (K. Tempest and S. Emerson, unpublished results, 2009). Equilibrium isotope solubilities were determined using the same methodology used to determine Ne and N$_2$ solubility values [*Hamme and Emerson*, 2004b]. The kinetic fractionation factors were determined by measuring the relative diffusion rate of the argon isotopes into gas-purged water under conditions of constant pressure and temperature. The experimental setup was identical to that described by *Knox et al.* [1992].

4.2. Gas Exchange Model

[23] Gases transfer between the ocean and atmosphere both by diffusive gas exchange and bubble processes. Bubble processes play an important role in gas exchange, particularly for relatively insoluble gases [e.g., *Hamme and Emerson*, 2006; *Stanley et al.*, 2006, 2009]. The air-sea gas flux (F_C) is the sum of both processes:

$$F_C = k_C\left([C] - [C]_{\text{sat}}\right) + B_C \tag{4}$$

where k_C is the gas transfer velocity that is often parameterized as a function of wind speed and Schmidt number [*Nightingale et al.*, 2000; *Wanninkhof*, 1992], and B_C represents the bubble flux. Each gas has unique values of k_C, $[C]_{\text{sat}}$, and B_C based on its physical properties. The relative piston velocities of two gases are related by their Schmidt number, Sc, to the power n [*Wanninkhof*, 1992]:

$$(k_1/k_2) \propto (Sc_1/Sc_2)^{-n} \tag{5}$$

where (Sc) is the ratio of the molecular diffusion coefficient (D), a property of each individual gas, to the kinematic viscosity (ν), a property of the liquid, both of which vary with temperature. The exponent n is believed to be approximately 0.5 for wind speeds above about 5 m s^{-1}, on the basis of laboratory experiments and theoretical calculations [*Jähne et al.*, 1987b; *Ledwell*, 1984; *Watson et al.*, 1991]. When

Table 2b. Physical Properties of Argon Isotopes[a]

	Values
Equilibrium Fractionation (‰)	
2°C	1.05
25°C	1.21
Kinetic Fractionation Isotope ($\alpha_k^{40/36}$)	
$\alpha_{40/36}$	0.995
Isotopic Abundance (%)	
^{40}Ar	99.60
^{36}Ar	0.337

[a]The seawater equilibrium for $^{40}Ar/^{36}Ar$ was determined in our laboratory by equilibrating fresh water at constant temperature and pressure for several weeks (S. Emerson et al., unpublished results, 2009). For this paper, equilibrium $\delta^{40}Ar$ fractionation as a function of temperature was taken to be a linear interpolation between these two values, with no salinity dependence. Kinetic fractionation was determined experimentally (K. Tempest and S. Emerson, unpublished results, 2009) in a manner similar to previous determinations for oxygen [*Knox et al.*, 1992].
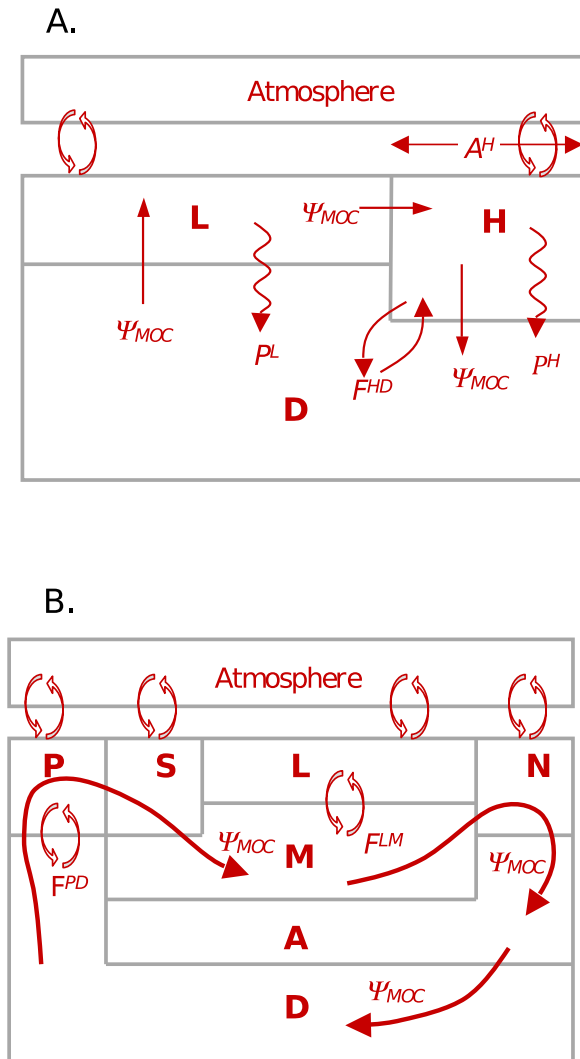
A.

B.

Figure 3. Schematic of the (a) three-box model and (b) seven-box model. Fluxes between boxes are represented by arrows. Each box model has an overturning circulation (ψ_{MOC}) of 20 Sv. Mixing fluxes between boxes are denoted F^{ij}, where the superscripts i and j indicate the two boxes that exchange water (e.g., F^{HD} refers to mixing between the H and D boxes). Sinking biological fluxes (e.g., P^H) transport phosphate, DIC, and alkalinity downward in a fixed ratio. Sinking arrows are not shown in the seven-box model diagram for clarity. The three-box model geometry is set according to *Sarmiento and Toggweiler* [1984], and the seven-box model is based on that of *Toggweiler* [1999]. The default surface area of the high-latitude box is 15% of total ocean surface area for the three-box model. For the seven-box model, default surface areas are 10% for box N and 5% for box P.

comparing the ratio of k_C for two gases or two isotopes of the same gas at the same temperature, the viscosity terms, ν, cancel. For example, the piston velocities of Ar and CO_2 are related at any given temperature as

$$\left(k_{Ar}/k_{CO2}\right) = \left(Sc_{Ar}/Sc_{CO2}\right)^{-0.5} = \left(D_{Ar}/D_{CO2}\right)^{0.5}. \quad (6)$$

The relative diffusivities, solubilities, and gas piston velocities for the inert gases and CO_2 are presented in Tables 2a and 2b. The gas piston velocity for ^{36}Ar was calculated on the basis of the kinetic isotope fractionation of $\alpha_k = 0.995$ as described above so that

$$\alpha_k^{40/36} = \frac{k_{40Ar}}{k_{36Ar}}. \quad (7)$$

[24] We parameterize the bubble flux as the sum of two end member processes [*Fuchs et al.*, 1987] which consists of small bubbles that completely collapse, injecting their entire contents into seawater (V_{inj}), and large bubbles that exchange diffusively while briefly submerged, before rising back to the surface (V_{ex}). The first process depends only on the injection rate and the mole fraction of the gas in the atmosphere, χ_C, while the exchange processes also depends on the solubility, β_C, and molecular diffusion rate of the specific gas,

$$B_C = \left(V_{inj} + V_{ex}D_C^x\beta_C^y\right)\chi_C. \quad (8)$$

Values of $x = 0.5$ and $y = 1$ were chosen following *Hamme and Emerson* [2006], but other researchers have used different exponents on the basis of whether one assumes clean or dirty bubble surfaces (see *Emerson and Hedges* [2008], chapter 9, for a review). Although the relative contribution of V_{inj} and V_{ex} is uncertain, recent studies have indicated that the ratio of the flux of exchanging bubbles is similar in magnitude to the flux from injecting bubbles for argon and oxygen [*Hamme and Emerson*, 2006], while others suggest that completely collapsing (V_{inj}) bubbles dominate [*Stanley et al.*, 2009]. We determined our results with a range of V_{inj} and V_{ex} values such that the ratio of the relative contribution of injecting to exchanging bubbles varied from 1/2 to 2/1. As a base case, we assign a ratio of unity to the magnitude of injecting and exchanging bubble fluxes for argon [*Emerson and Hedges*, 2008] such that

$$V_{ex} = \frac{D_{Ar}^{0.5}\beta_{Ar}}{V_{inj}}. \quad (9)$$

Generally, the model results were insensitive to the amount of exchanging bubbles because exchanging bubbles tended to raise the concentration of each gas proportionally, leaving gas ratios more or less unchanged.

4.3. Box Model Solutions

[25] We utilized a simple three-box model originally formulated in ST84 and a more complicated seven-box model [*Toggweiler*, 1999] to interpret our measured gas and isotope ratios in the deep sea (Figure 3). We explain our model solution, using the simple three-box model for conceptual clarity, and then demonstrate that the more complex seven-box model produces similar results.

[26] For both models we use measurements of inert gases and argon isotope ratios to constrain two variables, the high-latitude surface area, A^H, and the bubble injection flux, V_{inj}. For the seven-box model, we consider the high-latitude surface area, A^H, to be the sum of the two high-latitude boxes, $A^P + A^N$. We then evaluate how changing box model geometry on the basis of inert gas constraints influences the par-

Table 3. Three-Box and Seven-Box Model Default Parameters[a]

Parameter Name	Symbol	Value
Three-Box Model		
Low-latitude temperature (°C)	T^L	21.5
High-latitude temperature (°C)	T^H	2.5
Meridional overturning circulation (Sv)	Ψ_{MOC}	20
High-latitude mixing (Sv)	F^{HD}	42.8
Depth of high-latitude box (m)	z^H	250
Depth of low-latitude box (m)	z^L	100
Volume of atmosphere (mol)	V_{atm}	1.773×10^{20}
Volume of ocean (m³)	V_{oc}	1.292×10^{18}
Surface area of the ocean (m²)	A_{oc}	3.49×10^{14}
Alkalinity (μmol kg^{-1})	Alk	2371
fCO$_2$ of atmosphere (μatm)	fCO$_{2atm}$	280
Seven-Box Model		
North high-latitude temperature (°C)	T^N	3.0
North high-latitude temperature (°C)	T^S	8.0
North high-latitude temperature (°C)	T^P	1.0
Surface area north high-latitude box (%)	A^N	10
Surface area sub-Antarctic box (%)	A^S	10
Surface area south polar box (%)	A^P	5
Surface area low-latitude box (%)	A^L	100 − (A^N + A^S + A^P)
Mixing between P and D boxes (Sv)	F^{PD}	60
Mixing between L and M boxes (Sv)	F^{LM}	40
Depth of north high-latitude box (m)	z^N	250
Depth of south polar high-latitude box (m)	z^P	250
Depth of sub-Antarctic box (m)	z^S	250

[a]Three-box model parameters are from ST84. Carbon cycle parameters are for abiotic carbon system calculations. Seven-box model parameters are from *Toggweiler* [1999]. Values of V_{atm}, V_{oc}, A_{oc}, z^L, Ψ_{MOC}, Alk, and fCO$_{2atm}$ are all the same as in the three-box model.

titioning of CO$_2$ between the ocean and atmosphere in the three-box model.

4.3.1. Three-Box Model

[27] The three-box model is composed of an atmosphere box, a low-latitude surface box, a high-latitude surface box, and a deep ocean box (Figure 3a). The model features a meridional overturning circulation (Ψ_{MOC}) and gas exchange across the air-sea interface of the two surface boxes, including a bubble flux as described in equation (8). Gas transfer coefficients for high- and low-latitude boxes (k^H and k^L) were set to 3 m d^{-1} following ST84. Additionally, a high-latitude convection flux (F^{HD}) mixes water between high-latitude and the deep ocean. The pCO$_2$ of high- and low-latitude boxes are calculated from model T, S, dissolved inorganic carbon (DIC), and alkalinity (Alk) using the carbonate system formulation from *Zeebe and Wolf-Gladrow* [2001]. Parameters of the three-box model (Table 3) are the same as those of ST84 for the rest of this paper, except where specifically noted. ST84 assigned a value for the overturning circulation, Ψ_{MOC} to be 20 Sv based on ^{14}C mass balance [*Broecker and Peng*, 1982]. The mean high- and low-latitude surface temperatures were based on *Levitus* [1982] climatology where

the low-latitude box represents the region from 50°S to 60°N. Mean phosphate, alkalinity, and dissolved inorganic carbon concentrations in the boxes are based on averages of data from the Geochemical Ocean Sections program (GEOSECS).

[28] Inert gases were added to the three-box model, allowing us to calculate the steady state distribution of gas ratios in the deep ocean box. Gas transfer coefficients for the inert gases were determined relative to CO$_2$ on the basis of Schmidt number dependence (equation (5); Table 2a). To derive the steady state solution, we start by writing two independent equations. The first represents conservation of gas mass in the high-latitude box. Since the only source of gas input to the deep ocean is from the high-latitude box via Ψ_{MOC} and F^{HD}, the gas concentration in the deep box must be equal to that of the high-latitude box. Therefore, F^{HD} does not influence the mass balance of the high-latitude or deep ocean boxes because it exchanges water with the same gas concentration. The mass balance of an inert gas in the high-latitude box is then set by a balance between input via gas exchange and loss via the meridional overturning circulation, which in steady state balances as follows:

$$0 = \psi_{MOC}\left([C]^L - [C]^H\right) + A^H\left(-k_C^H\left([C]^H - [C]_{sat}^H\right) + B_C^H\right) \quad (10)$$

where superscripts denote the box (H = high latitude, L = low latitude) and B_C is the bubble flux from equation (8).

[29] A second equation requires the total air-sea gas flux to be zero:

$$0 = A^L\left(-k_C^L\left([C]^L - [C]_{sat}^L\right) + B_C^L\right) + A^H\left(-k_C^H\left([C]^H - [C]_{sat}^H\right) + B_C^H\right). \quad (11)$$

Equation (10) and equation (11) are combined to solve for the concentration of a gas in the low $[C]^L$ and high $[C]^H$ latitude surface boxes. By rearranging equation (10) and calculating the gas saturation anomaly of the high-latitude box (ΔC^H) relative to atmospheric equilibrium we gain insight into the effect of cooling, bubble fluxes, and gas exchange on setting the disequilibrium in the high-latitude box

$$\Delta C^H = \underbrace{\frac{\psi_{MOC}\left([C]^L - [C]^H\right)}{[C]_{sat}^H \, A^H k_C^H}}_{\text{Cooling component}} + \underbrace{\frac{B_C^H}{[C]_{sat}^H \, k_C^H}}_{\text{Bubble component}}. \quad (12)$$

[30] Intuition on the role of cooling can be gained by conceptualizing a water parcel moving poleward at the surface. The parcel starts with a relatively high temperature, and a low gas concentration ($[C]^L$), but as it moves poleward, the parcel is cooled, increasing its capacity to hold gas ($[C]_{sat}^H$), a demand that is met by an air-sea flux of gas (proportional to $A^H k^H$) into the parcel. The parcel is then subducted before it can fully equilibrate, making the cooling component negative for the high-latitude box. The magnitude of $[C]^L - [C]^H$ depends both on the physical properties of the gas, as well as the temperature difference between the high- and low-latitude boxes. As the term $A^H k^H$ increases, gas exchange forces the system back toward equilibrium and reduces the magnitude of the undersaturation. The cooling disequilibrium is thus a balance between cooling, which creates under-
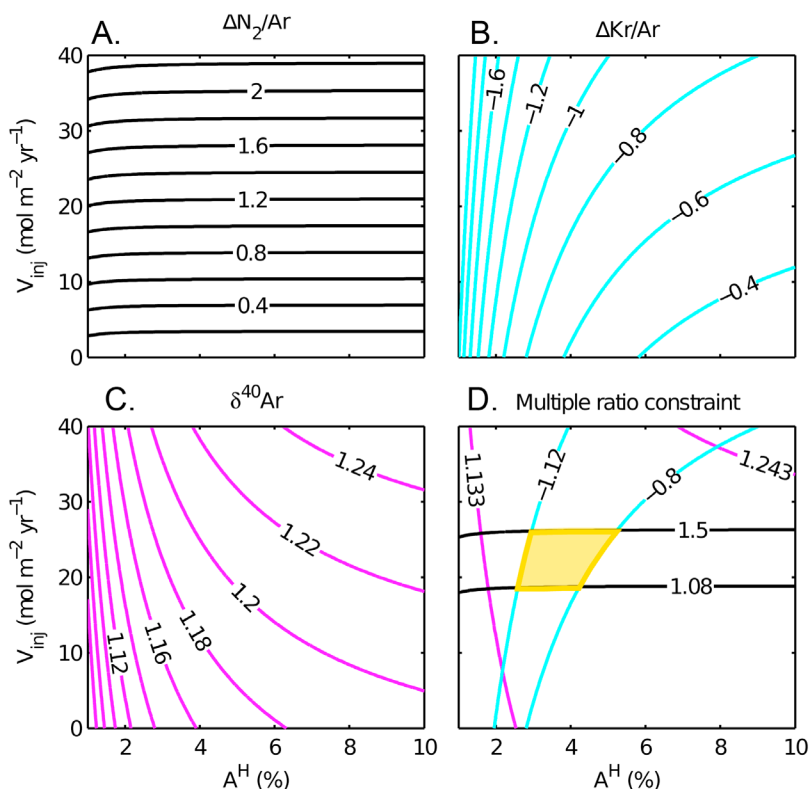
Figure 4. Three-box model solution for gas ratios with contours for (a) $\Delta N_2/Ar$ (black), (b) $\Delta Kr/Ar$ (cyan), and (c) $\delta^{40}Ar$ (magenta) calculated for a range of values of high-latitude surface area, A^H (in percent of ocean surface area), and bubble injection flux, V_{inj}. (d) The contours represent the range of observed gas ratios in deep ocean samples: $1.29\% \pm 0.21\%$ for $\Delta N_2/Ar$, $-0.96\% \pm 0.16\%$ for $\Delta Kr/Ar$, and $1.188‰ \pm 0.055‰$ for $\delta^{40}Ar$. Only a small region of the parameter space is consistent with all three proxies (gold region). This region corresponds to a surface area of 2.6%–5.2% and a bubble injection flux of 19–26 mol m^{-2} yr^{-1}.

saturation, and the rate of gas exchange, which reduces the undersaturation. When circulation is faster (slower) and high-latitude surface area is smaller (larger), the magnitude of the cooling undersaturation is larger (smaller).

[31] The bubble component is the balance between the rate of the positive bubble flux and gas exchange. The bubble component does not depend on A^H because both B_C^H and k_C^H scale equally with A^H, and it cancels. For a given bubble flux a less soluble gas will have a larger percent bubble supersaturation. Increasing the rate of gas exchange drives ΔC toward zero. The saturation anomaly of heavy, soluble gases (e.g., Kr) tends to be dominated by cooling-induced undersaturation, while light, less soluble gases (e.g., Ne) have positive saturation anomalies due to bubbles [*Hamme and Severinghaus*, 2007].

[32] Using equations (10) and (11), the gas and isotope ratios (Kr/Ar, N$_2$/Ar, and $\delta^{40}Ar$) of the deep box can be determined as a function of A^H and V_{inj}. Each gas and isotope ratio was solved for a whole range of A^H and V_{inj} values in the three-box model, and the solution contoured (Figure 4). The orientation of the gas ratio contours in Figure 4 is controlled by a balance between the cooling and bubble components of equation (12). Decreasing A^H increases the relative importance of the cooling anomaly while increasing V_{inj} increases the importance of the bubble component. For the high-latitude gas ratio saturation anomaly of any two gases, $\Delta C_1/$

C_2 (as defined in equation (2)), the cooling component of $\Delta C_1/C_2$ is negative when the solubility of C_1 is more temperature dependent than C_2, resulting in ΔC_1 being more negative than ΔC_2. The bubble-induced supersaturation is greater for less soluble gases because the gas is relatively enriched in the atmosphere compared to water. Since the bubble-induced supersaturation is independent of the area A^H, the top of Figures 4a–4d are bubble dominated, while the lower corners of Figures 4a–4d is the cooling-dominated extreme. A smaller gas exchange mass transfer coefficient, k, also increases bubble-induced supersaturation because the slower gas exchange rate is less able to moderate the supersaturation back toward equilibrium. For N$_2$/Ar and Kr/Ar, differences in solubility and the temperature dependence of solubility are much greater than differences in k, and solubility properties primarily determine contour orientation. On the other hand, for $^{40}Ar/^{36}Ar$ the temperature dependence of solubility for the two isotopes is very similar, and the difference in k between isotopes is more important.

[33] $\Delta N_2/Ar$ contours (Figure 4a) are primarily horizontal and increase with increasing bubble flux, indicating that the bubble component dominates over the cooling component. This is because N$_2$ is less than half as soluble as Ar, while the two gases have similar temperature dependence of solubility and similar k values (Tables 2a and 2b). A larger V_{inj} increases [N$_2$] more than [Ar], resulting in a larger $\Delta N_2/Ar$ (Figure 4a).

In contrast, for $\Delta Kr/Ar$, the solubility-temperature dependence of Kr is greater than that for Ar, leading to a larger cooling anomaly for Kr than for Ar, causing $\Delta Kr/Ar$ to become more negative as A^H decreases (Figure 4b). At the same time, Ar is about half as soluble as Kr, so $\Delta Kr/Ar$ becomes smaller (more negative) for larger V_{inj}. Both cooling and bubbles thus make $\Delta Kr/Ar$ more negative, and the contours cross those of $\Delta N_2/Ar$ as A^H decreases.

[34] The $\delta^{40}Ar$ in saturation equilibrium with the atmosphere at 2.5°C is 1.21‰ relative to the atmosphere. Cooling of the surface water during deepwater formation causes argon undersaturation and induces invasion from the atmosphere. Since ^{36}Ar has a larger molecular diffusion rate than ^{40}Ar $((D^{36}/D^{40})^{0.5} \sim 1.005)$, gas invasion causes the isotope ratio in the surface waters to become lighter (more negative) with respect to the atmospheric value. As the area decreases, the degree of argon undersaturation and invasion increases, and thus the $\delta^{40}Ar$ value decreases toward the left side of Figure 4c. The influence of bubble injection on $\delta^{40}Ar$ is determined by the balance of two effects. The first is that bubbles increase the saturation state of the surface ocean, thus reducing diffusive ingassing which causes a decrease in the magnitude of lightening caused the kinetic isotope effect described above. This effect makes $\delta^{40}Ar$ heavier with increasing bubble flux. The second effect is that argon in the bubbles being injected have the $\delta^{40}Ar$ of air (0‰), which is about 1‰ lighter than in the water. The competing effects of injecting lighter values of $\delta^{40}Ar$ and creating heavier values because of kinetic fractionation during diffusive exchange partially cancel, but the kinetic fractionation effect is larger, and therefore, the net effect is that $\delta^{40}Ar$ increases with increasing bubble injection flux.

[35] A combination of the solutions for the three gas and isotope ratios is presented in Figure 4d. The contours show the error bounds of measured deep ocean mean values for each gas ratio. The shaded region where all three ratios overlap represents the parameter space consistent with all three constraints and corresponds to a surface area, A^H, of 2.6%–5.2% of ocean surface area and a bubble injection rate, V_{inj}, of 19–26 mol m^{-2} yr^{-1}. Our solution region is also consistent with previous $\Delta Ne/Ar$ and $\Delta Kr/Ar$ measurements below 2000 m at HOT of 2.5% ± 0.4% [Hamme and Emerson, 2004a] and −0.83‰ [Hamme and Severinghaus, 2007]. To evaluate the sensitivity of the solution to the choice of model parameters, we incorporated uncertainty in parameter values for Ψ_{MOC}, k^H, and $(T^H - T^L)$ and in the $V_{inj}:V_{ex}$ ratio (see later discussion in section 4.4).

[36] Given present analytical uncertainties, $\Delta N_2/Ar$ and $\Delta Kr/Ar$ provide the best constraint, but an attainable improvement in precision of measuring $\delta^{40}Ar$ could enhance its utility as a tracer. Having more than two gas ratios provides a check against the possibility that additional processes not considered also influence the observations. For example, denitrification has been demonstrated to elevate $\Delta N_2/Ar$ in certain regions [Devol et al., 2006] and could possibly contribute to the bulk deep ocean $\Delta N_2/Ar$. Ice-ocean interactions could also modify inert gas ratios, particularly for light gases [Hamme and Emerson, 2002].

4.3.2. Seven-Box Model

[37] The three-box model of ST84 provides a simple and intuitive solution. We have also applied the inert gas constraints to a more realistic seven-box model [Toggweiler, 1999]. The seven-box model was constructed by Toggweiler [1999] to better explain glacial/interglacial changes in atmospheric pCO_2, as well as deep ocean ^{13}C and nutrient paleorecords. The model includes distinct northern and southern deepwater formation regions and has separate boxes analogous to North Atlantic deep water (NADW) and Antarctic bottom water (AABW) (Figure 3b). We solved the seven-box model for our inert gas tracers and constrained the bubble flux and surface area both for the northern high-latitude box (N) and the southern polar box (P) by comparing the A box to our Atlantic observations and the D box to our Pacific observations (see Appendix B). The best fit parameter values were $V_{inj}^N = 16.9$ mol m^{-2} yr^{-1}, $V_{inj}^P = 29.8$ mol m^{-2} yr^{-1}, $A^P = 0.6\%$ and $A^N = 2.6\%$. The total high-latitude surface area $(A^P + A^N)$ of the optimal solution was 3.2% and compared well with the results from the deep box of the three-box model. For both three- and seven-box models, $\Delta Kr/Ar$ proved to be more useful than $\delta^{40}Ar$ for constraining high-latitude surface area, given the range of deep ocean values we observed (Figure 5).

[38] The added complexity of the seven-box model offers further insight into the relative role of northern and southern high-latitude regions in setting the gas composition of the deep ocean. Observed $\Delta N_2/Ar$ in the Pacific was higher than in the Atlantic, while both basins had similar $\Delta Kr/Ar$. The lower observed $\Delta N_2/Ar$ values in the Atlantic relative to the Pacific resulted in a significantly smaller air-sea bubble flux in the N box (which feeds the deeper A box) compared with the P box. Although observed $\Delta Kr/Ar$ of the deep ocean did not appear to vary between basins, the results of the seven-box model suggest that the observed negative $\Delta Kr/Ar$ in the A versus D boxes were composed of different relative contributions of cooling and bubble injection, both of which make $\Delta Kr/Ar$ more negative. If the bubble effect is removed, $\Delta Kr/Ar$ caused by cooling alone was 0.7% for the A box and 0.6% for the D box, implying a slightly greater cooling signal in the north and a smaller cooling component (but more bubbles) in the south.

[39] In the optimal model solution, high-latitude surface area was dominated by the N box, where the southern P box had only a very small outcrop (0.6%), perhaps comparable to the very small regions where AABW is actively formed. Despite a small outcrop, the P box strongly contributed to the composition of the deep ocean via convection. For example, $\Delta N_2/Ar$ of the deep D box (1.33%) was closer to the P box value (1.45%) than to the N box value (0.95%).

[40] The very small A^P (0.6%) of the best fit solution, however, was quite sensitive to assumed model circulation. Although the total high-latitude surface area $(A^P + A^N)$ was robust to changes in model parameters, the relative surface areas of P and N boxes were sensitive to assumed model circulation parameters. For example, if mixing between D and A boxes (F^{AD}) was added, the best fit surface area increased for A^P and decreased and A^N (Figure 6). Changing F^{AD}, however, had a large impact on the predicted $\Delta N_2/Ar$ of the P and N boxes. More observations of the northern and southern end-members are needed to better constrain the relative contribution of the north versus south to the solubility pump of the deep ocean.
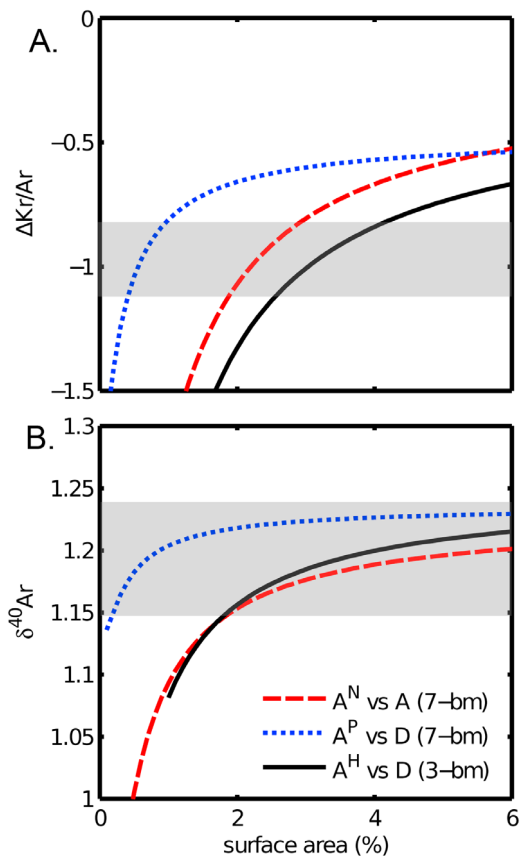
Figure 5. Seven-box and three-box model simulations of (a) $\Delta Kr/Ar$ and (b) $\delta^{40}Ar$ for varying the surface area of high-latitude boxes (A^N, A^P, and A^H). Bubble injection flux was fixed at 22.7 mol m^2 yr^{-1} for the three-box model and 17.1 and 29.6 mol m^2 yr^{-1} for the N and P boxes of the seven-box model, respectively. For the seven-box model, first A^N was varied while holding A^P constant at 0.6% (dashed lines), then A^P was varied while holding A^P constant at 2.6% (dotted lines). Figure 5a shows the $\Delta Kr/Ar$ of A box as a function of A^N (dashed), $\Delta Kr/Ar$ of D box as a function of A^P (dotted), and $\Delta Kr/Ar$ of D box as a function of A^H for three-box model (black line). Figure 5b is the same as Figure 5a but for $\delta^{40}Ar$. Mean deep ocean measured values are shown in grey shading.

4.4. Sensitivity Analyses

[41] The box model solutions depend on a number of assumed model parameters. These include the overturning circulation rate, Ψ_{MOC}, The temperature difference between high and low latitudes, ($T^H - T^L$), the high-latitude gas transfer velocity, k_C^H, and the bubble exchange ratio, V_{ex}. We test the sensitivity of our solution to each of these parameters by varying each parameter, one at a time, from two thirds to 3/2 of their initial values and determining the best fit for A^H and V_{inj} on the basis of mean deep ocean $\Delta N_2/Ar$ and $\Delta Kr/Ar$ constraints (Figure 7). Varying each of these parameters caused A^H in the three-box model to vary between 2.7% and 5.3%. The only parameter that V_{inj} is sensitive to is k_C^H. Increasing k_{CO2}^H from 2 to 4.5 m d^{-1} resulted in the value for

V_{inj} increasing from 15 to 33 mol m^{-2} yr^{-1}. Results for the seven-box model were similar, but with slightly lower total high-latitude surface area (Figure 7).

[42] The simplicity of the box models makes them easy to solve many thousands of times. In another sensitivity analysis, we calculated the confidence intervals for the three-box and seven-box model solution using a Monte Carlo approach. First, only the uncertainty in measured deep ocean gas ratios is considered. For the three-box model, $\Delta Kr/Ar$ and $\Delta N_2/Ar$ are each assigned a random value from a normal distribution with the mean and standard deviation of our mean deep ocean measurements ($\Delta Kr/Ar = -0.95\% \pm 0.16\%$ and $\Delta N_2/Ar = 1.29\% \pm 0.21\%$). A^H and V_{inj} were then calculated from the randomly selected values ($\pm 1\sigma$). This process was repeated 5000 times to produce a distribution of A^H and V_{inj} values such that $A^H = 3.6\%$ (+1.3%, −0.8%) and $V_{inj} = 22.5$ (+3.7, −3.6) mol m^{-2} yr^{-1}. Error bounds are asymmetric and represent values that encompass one standard deviation of the resulting values. For the seven-box model, the same procedure was followed, except instead of using the whole ocean deep mean values, box model $\Delta Kr/Ar$ and $\Delta N_2/Ar$ results for the A box were compared to the deep mean of BATS
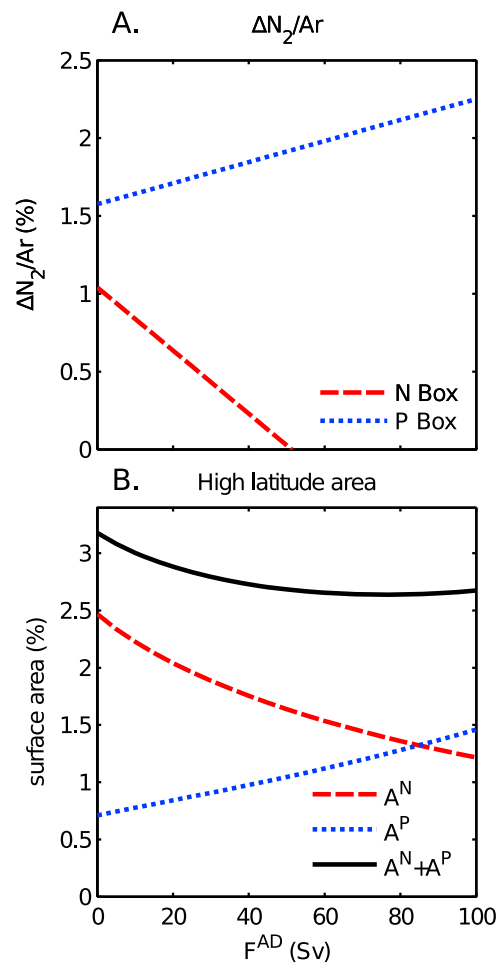

Figure 6. Seven-box model sensitivity to mixing between A and D boxes (F^{AD}). (a) $\Delta N_2/Ar$ in the N and P box as a function of F^{AD}. (b) Best fit solution for the surface area of N and P boxes as a function of F^{AD}.
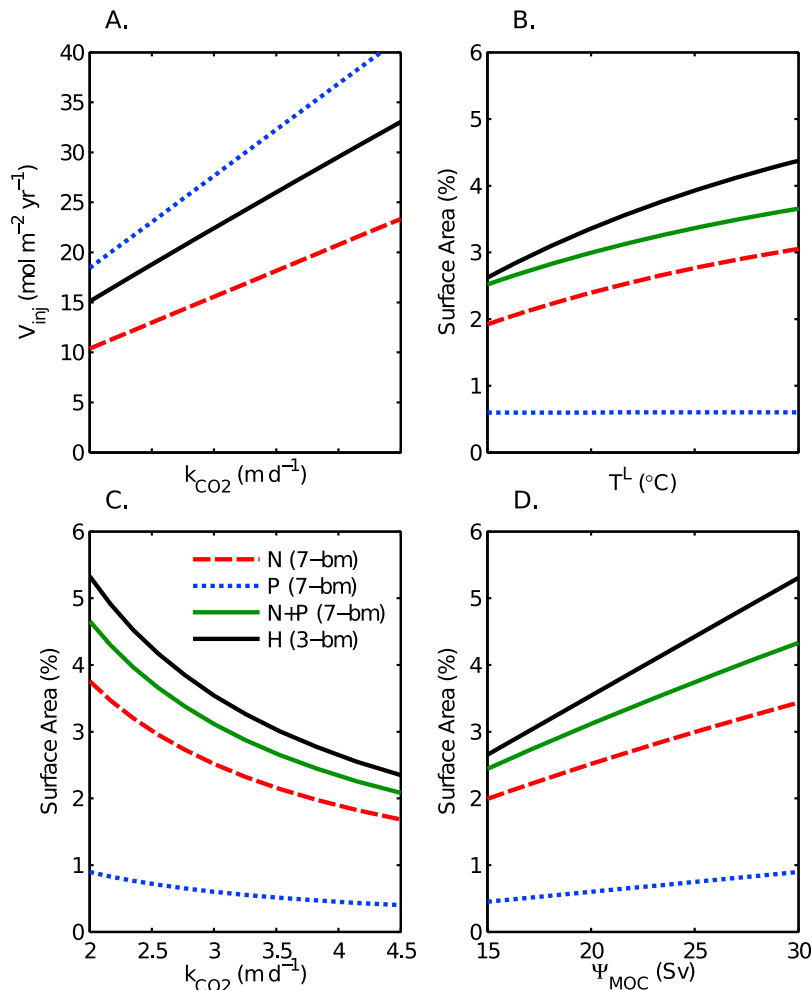
Figure 7. The sensitivity of the box model solutions for the three-box model (black) and the seven-box model (red, blue, and green). (a) Bubble injection rate, V_{inj}, as a function of gas transfer velocity, k^H. (b) High-latitude surface area, A^H, as a function of low-latitude temperature (T^L). (c) A^H as a function of k^H and (d) A^H as a function of the overturning circulation, Ψ_{MOC}. The dashed and dotted lines are the results for the N box and P box of the seven-box model, respectively. The solid green line is the sum of the surface area of the N and P boxes.

and ETA observations, while results from the D box were compared to the deep mean of HOT, STNP, and NWP observations. Surface area for the north (N) and south polar box (P) was $A^N = 2.6\%$ (+0.9%, −0.6%) and $A^P = 0.6\%$ (+0.4%, −0.2%), resulting in a total high-latitude surface area of $A^H = 3.4\%$ (+0.9%, −0.6%). Bubble injection was $V^N = 17.0$ (+1.4, −1.5) mol m^{-2} yr^{-1} and $V^P = 29.7$ (+3.5, −3.0) mol m^{-2} yr^{-1} for the N and P boxes, respectively. Error bounds were calculated as the range containing 68% of values.

[43] The Monte Carlo approach was then extended to include uncertainties in box model parameters in addition to the assigned uncertainty in gas ratios. Ψ_{MOC}, $(T^H − T^L)$, k_C^H, and V_{ex} are each assigned a random value from a normal distribution around base case values assuming a ±30% error in each term. Parameters were randomly selected 5000 times and A^H and V_{inj} were then calculated from the resulting distribution. A^H was 3.6% (+2.5%, −1.7%) while V_{inj} was 22.7 (+8.8, −7.3) mol m^{-2} yr^{-1}. For the seven-box model, surface area was $A^N = 2.6\%$ (+1.8%, −1.0%), $A^P = 0.6\%$ (+0.6%, −0.3%), and $A^H = 3.3\%$ (+2.2%, −1.3%), and

bubble injection rate was $V^N = 17.1$ (+6.1, −4.8) mol m^{-2} yr^{-1} and $V^P = 29.6$ (+10.8, −8.4) mol m^{-2} yr^{-1}.

5. Conclusions

5.1. Bubble Fluxes

[44] Bubble injection fluxes are less important for soluble gases such as CO_2 but essential to the gas cycling of less soluble gases, including O_2. Earlier, we described bubbles in the ocean in terms of two end-members: completely collapsing bubbles and diffusive exchanging bubbles. Our geochemical constraints are insufficient to evaluate the contribution of exchanging bubbles but provide strong constraints on the rate of the injecting bubble end-member (V_{inj}).

[45] The influence that bubbles have on the inert gas saturation anomaly depends on the magnitude of the gas piston velocity as described in the "bubble component" in equation (12). Our results are based on the gas transfer k values in Tables 2a and 2b, originally from ST84, which can be translated to wind speed on the basis of the choice of wind

speed parameterization to be, for example, 9.12 m s^{-1} [*Nightingale et al.*, 2000] or 8.14 m s^{-1} [*Wanninkhof*, 1992]. If, as is likely, wind speeds during deepwater formation were higher, our bubble flux is an underestimate of true high-latitude bubble injection flux.

[46] The mean injection flux of 27.2 mol m^{-2} yr^{-1} calculated for deepwater formation during winter by *Hamme and Severinghaus* [2007] was greater but with error of our result from the three-box model (22.7 mol m^{-2} yr^{-1}) and comparable to our result for the P box of the seven-box model (29.6 mol m^{-2} yr^{-1}). In the subtropical Pacific, at HOT, bubble injection calculated from inert gases was found to be smaller, at 6.2 mol m^{-2} yr^{-1} [*Hamme and Emerson*, 2006]. The lower injection flux is likely due to lower wind speeds in the subtropics compared to the high-latitude regions that ventilated our deep ocean samples. *Stanley et al.* [2009] suggested a wind speed cubed parameterization for bubble injection on the basis of observations at BATS. Using the *Stanley et al.* [2009] parameterization, bubble injection flux is 25.7 mol m^{-2} yr^{-1} at $u_{10} = 8.14$ m s^{-1} and 40.8 mol m^{-2} yr^{-1} at $u_{10} = 9.12$ m s^{-1}. Our bubble injection estimates thus fall between the results of *Stanley et al.* [2009] and *Hamme and Emerson* [2006]. When compared to our result, the *Stanley et al.* [2009] parameterization appears to overestimate bubble injection at high latitudes. This mismatch may not be surprising, given the rapid increase of both V_{inj} and k with wind speed, and the fact that the *Stanley et al.* [2009] parameterization is based on subtropical observations. Our results greatly expand the number of inert gas measurements from locations that outcrop at high latitudes, which is essential to improving our understanding of air-sea bubble fluxes at higher wind speeds. To further our progress, though, requires a careful analysis of the spatial variability in wind speed, ventilation pathways and mixing that is beyond the scope of our box-modeling approach. In general, the variability between studies and study regions highlights the challenge in parameterizing bubble fluxes based solely on wind speed.

5.2. Carbon Cycle Sensitivity

[47] Changing the geometry of the box models can have large impacts on the strength of the solubility pump of these models. In both the three-box and seven-box models, a solubility-only (biology turned off) carbon cycle was calculated using the surface areas as constrained by inert gases. The smaller high-latitude surface area decreased the effectiveness of the carbon solubility pump which in turn decreased the surface to deep DIC gradient (DIC^D − DIC^L) and increased the air-sea pCO$_2$ gradient of the high-latitude box.

[48] T03 measured the strength of the solubility pump in a GCM and found that the deep ocean had a total dissolved inorganic carbon concentration that was about 75 μmol kg^{-1} less than the equilibrium capacity of the deep water. On the basis of observations of an air-sea pCO$_2$ deficit of 60–70 ppm near NADW formation regions and the assertion that the deficit should be less in the Southern Ocean, T03 argued that the real ocean should have a smaller deficit (stronger solubility pump) than indicated by the GCM result. T03 hypothesized that the three-box model with a surface area of about 6% should best represent the true solubility pump.

[49] Our inert gases suggest a smaller surface are of 3.6%. With this surface area, the three-box model had a deep ocean DIC of 70 μmol kg^{-1} below equilibrium. The seven-box model with 3.2% of surface area in high-latitude boxes had a deep DIC deficit of 60 μmol kg^{-1}. In the constrained box models, the carbon solubility pump was slightly stronger than the GCM, weaker than hypothesized by T03, and much weaker than the default geometry for the three- and seven-box models, which had DIC deficits of 25 and 16 μmol kg^{-1}, respectively.

[50] Our results could be explained if the Southern Ocean has a larger solubility-induced pCO$_2$ deficit than previously believed or if the observed pCO$_2$ deficits in NADW formation regions are influenced by a contribution of biologically remineralized carbon and are thus not representative of the solubility deficit. Another possibility is if intermediate water formation contributes a significant cooling signal to the deep ocean, which is not resolved by the box models. Additional inert gas measurements that directly sample Antarctic bottom water and NADW could better illuminate this discrepancy.

[51] An important caveat to using inert gases to make conclusions about CO$_2$ is the relative time scales of CO$_2$ and inert gas equilibration with respect to gas exchange. CO$_2$ has an equilibration time scale of about a year, compared to inert gases, which have a time scale on the order of a month. In our box models, surface forcing is constant and all gases reach a steady state solution. Because of seasonality in the real ocean, equilibration of CO$_2$ in subducting water depends more on conditions over the annual cycle while inert gases would be more influenced by winter conditions. Thus, the inert gases provide specific information about conditions during the final winter before subduction. The longer gas exchange residence time for CO$_2$ means that circulation effects are more important for CO$_2$. Also, if water is ventilated for a period less than a year, noble gases may have time to reach a steady state disequilibrium, but CO$_2$ may not. Because the residence time of each box, even when high-latitude surface area is reduced, is at least a few years and forcing is constant, the box model does not take these dynamics into account, and a GCM may be needed to resolve such effects.

6. Summary

[52] Inert gas and isotope tracer δ^{40}Ar, ΔKr/Ar and ΔN$_2$/Ar in the deep ocean had measured mean values of 1.188‰ ± 0.055‰, −0.96% ± 0.16%, and 1.29% ± 0.21%, respectively. Because these values do not vary greatly from ocean to ocean or with depth, box models may be rich enough in complexity to yield the most important factors controlling their concentrations. These measurements constrain the bubble injection flux (22.7 (+8.8, −7.3) mol m^{-2} yr^{-1}) and area of the high-latitude surface (3.6% (+2.5%, −1.7%)) in the three-box model. Using the seven-box model, V_{inj} was partitioned to a bubble flux of 29.6 mol m^{-2} yr^{-1} in the southern polar box and 17.1 mol m^{-2} yr^{-1} in the north. A^H was divided into 2.6% surface area in the north and 0.6% in the south. Given present analytical accuracy, the combination of ΔKr/Ar and ΔN$_2$/Ar were the best at resolving these properties although, with a modest improvement in precision, δ^{40}Ar would further improve upon the constraints given by ΔKr/Ar and ΔN$_2$/Ar.

[53] By adding observational constraints to model geometry, inert gas observations can be used to improve box models and more accurately determine the strength of the carbon solubility pump. Our inert gas observations suggest

Table A1. All δ^{40}Ar and ΔKr/Ar Measurements[a]

Depth (m)	δ^{40}Ar (‰)	ΔKr/Ar (%)
Eastern Tropical Atlantic, August 2008		
1	0.6959	−0.6979
1	0.6729	−0.5543
500	1.1993	−0.0730
500	1.2488	0.0723
1000	1.1729	−0.6193
1000	1.1716	−0.6529
1500	1.2111	−0.9508
1500	1.1867	−0.9263
2000	1.2094	−0.7560
2000	1.2083	−0.9010
2500	1.1705	−0.6597
2500	1.1876	−0.6958
3000	1.2128	−0.9523
3000	1.2347	−1.1769
4000	1.2175	−1.0238
4000	1.2614	−1.1454
4500	1.2735	−0.2964
4500	lost	lost
5000	1.3105	−0.9589
5000	1.3333	−0.9013
5300	1.2620	−0.7500
5300	1.2690	−0.9957
Northwest Pacific, October 2007		
470	1.2229	−0.7621
470	lost	lost
970	1.2067	−0.6511
970	1.2106	−0.8248
1930	1.1710	−0.8109
1930	1.2805	−0.8608
2930	1.1633	−1.1801
2930	1.2016	−0.8614
700	1.2080	−0.5229
700	1.1765	−0.4991
1400	1.1614	−0.7440
1400	1.1245	−0.8021
2400	1.1908	−0.8797
2400	1.1906	−0.8045
3500	1.1968	−0.9010
3500	1.1240	−0.9742
4500	1.1434	−0.9207
4500	1.1636	−1.1975
Subtropical North Pacific, September 2008		
2000	–	−0.8428
2000	–	−0.9374
3000	–	−1.0533
4000	–	−1.0899
4000	–	−1.0365
4500	–	−1.3509
4500	–	−0.9083
Hawaii Ocean Time Series, April 2001		
10	1.056	–
10	1.019	–
10	1.058	–
Hawaii Ocean Time Series, May 2001		
3	1.086	–
3	1.066	–
3	1.048	–
3937	1.197	–
3937	1.204	–
3937	1.216	–
Hawaii Ocean Time Series, November 2002		
4000	1.121	–
4000	1.123	–
4000	1.118	–
Hawaii Ocean Time Series, March 2003		
4000	1.126	–
4000	1.136	–

[a]Samples lost during measurement or sampling are denoted "lost."

that the carbon solubility pump has a significant level of inefficiency that transports a deficit of about 60–70 μmol kg^{-1} DIC into the deep ocean. The calculated solubility pump disequilibrium is comparable but slightly less than the 75 μmol kg^{-1} DIC of a GCM simulation (T03) and much greater than the default configuration of the three- and seven-box models (25 μmol kg^{-1} DIC and 16 μmol kg^{-1} DIC, respectively).

[54] As demonstrated with our box model results, properly representing high-latitude ventilation is an essential component to achieving accurate sensitivities in the carbon cycle. Challenging GCMs with the noble gas constraints may be best way to resolve the uncertainty in the strength of the solubility pump, and the relative contribution of northern and southern deepwater formation regions. The observations presented here, as well as future sampling of formation regions, can lead to better a representation of the carbon cycle in models. Such improvements are necessary to understand how the ocean and gas exchange regulate atmospheric pCO$_2$ both on glacial/interglacial and anthropogenic timescales.

Appendix A

[55] All δ^{40}Ar and ΔKr/Ar measurements are given in Table A1. Each line represents an individual sample flask. Dates listed are dates when samples were collected. Samples lost during measurement or sampling are denoted "lost." All samples collected from 2007 and 2008 were analyzed at the University of Washington, Seattle, Washington. Samples from 2001–2003 were analyzed at Scripps Institute of Oceanography, San Diego, California and at Institut Pierre Simon Laplace, Commissariat à l'Énergie Atomique, Saclay, France.

Appendix B: Seven-Box Model Methods

[56] The seven-box model has the same overturning rate of 20 Sv as the three-box model. A convection term, F^{DP}, exchanges water between the southern polar box and the deep ocean at a rate of 60 Sv. In the default configuration, the northern high-latitude box (N) has a surface area of 10% of total ocean surface area, and the southern polar box (P) has 5% of ocean surface area. Both of these high-latitude boxes contribute to the composition of the deep ocean box (D) while the deep (A) box is fed only by water coming from the N box. (Figure 3b). Deep water in the northern box is cooled while subducting, unlike the southern polar box (P), which communicates with the deep ocean via a convective mixing flux, F^{PD}. Like for the three-box model, the air-sea flux for all surface boxes was set as described in equations (4) and (8).

[57] The seven-box model was solved for the inert gases by simultaneously solving seven mass equations, one for each ocean box. The seven-box model has two high-latitude boxes in communication with the deep ocean (N and P). Our goal was to constrain bubble injection rate (V_{inj}^{N} and V_{inj}^{P}) and surface area (A^{N} and A^{P}) for each. To find an optimal solution for the seven-box model, these four parameters were allowed to vary to find the combination of parameter values that best matched deep ocean observations. For bubble injection, values for the N box (V_{inj}^{N}) and P box (V_{inj}^{P}) were varied independently while bubble injection for the S and L boxes were set to equal V_{inj}^{P} and V_{inj}^{N}, respectively. Gas ratios in the

deep ocean (D and A boxes) were not sensitive to the rate of bubble injection in S and L boxes. For surface area, A^P and A^N were varied independently while A^S was fixed at its default size, and A^L varied in size to preserve total ocean surface area.

[58] For each set of parameter values, the model solution for the A box was compared to the deep mean of observed $\Delta Kr/Ar$ and $\Delta N_2/Ar$ from ETA and BATS while the deep box was compared to the deep mean from Pacific data (NWP, HOT, STNP). Goodness of fit was considered to be the root-mean-squared difference between model and observed values where the magnitude of misfit for each gas ratio was scaled relative to the standard deviation of observed values. The seven-box model was solved for gas ratios with varying values of V_{inj}^N, V_{inj}^P, A^P and A^N to find the optimal parameters to reproduce observed deep ocean measurements.

References

Archer, D. E., G. Eshel, A. Winguth, W. Broecker, R. Pierrehumbert, M. Tobis, and R. Jacob (2000), Atmospheric *p*CO₂ sensitivity to the biological pump in the ocean, *Global Biogeochem. Cycles*, *14*(4), 1219–1230, doi:10.1029/1999GB001216.

Archer, D. E., P. A. Martin, J. Milovich, V. Brovkin, G. K. Plattner, and C. Ashendel (2003), Model sensitivity in the effect of Antarctic sea ice and stratification on atmospheric *p*CO₂, *Paleoceanography*, *18*(1), 1012, doi:10.1029/2002PA000760.

Broecker, W. S., and T. Peng (1982), *Tracers in the Sea*, Lamont-Doherty Geol. Obs., Columbia Univ., Palisades, New York.

Devol, A. H., A. G. Uhlenhopp, S. W. A. Naqvi, J. A. Brandes, D. A. Jayakumar, H. Naik, S. Gaurin, L. A. Codispoti, and T. Yoshinari (2006), Denitrification rates and excess nitrogen gas concentrations in the Arabian Sea oxygen deficient zone, *Deep Sea Res. Part I*, *53*(9), 1533–1547, doi:10.1016/j.dsr.2006.07.005.

Emerson, S., and J. Hedges (2008), *Chemical Oceanography and the Marine Carbon Cycle*, Cambridge Univ. Press, Cambridge, U. K.

Emerson, S., C. Stump, D. Wilbur, and P. Quay (1999), Accurate measurement of O₂, N₂, and Ar gases in water and the solubility of N₂, *Mar. Chem.*, *64*(4), 337–347, doi:10.1016/S0304-4203(98)00090-5.

Fuchs, G., W. Roether, and P. Schlosser (1987), Excess ³He in the ocean surface layer, *J. Geophys. Res.*, *92*(C6), 6559–6568, doi:10.1029/JC092iC06p06559.

Gildor, H., and E. Tziperman (2001), A sea ice climate switch mechanism for the 100-kyr glacial cycles, *J. Geophys. Res.*, *106*(C5), 9117–9133, doi:10.1029/1999JC000120.

Glueckauf, E. (1951), The composition of atmospheric air, in *Compendium of Meteorology*, edited by T. F. Malone, pp. 1–11, Am. Meteorol. Soc., Boston.

Hamme, R. C., and S. R. Emerson (2002), Mechanisms controlling the global oceanic distribution of the inert gases argon, nitrogen and neon, *Geophys. Res. Lett.*, *29*(23), 2120, doi:10.1029/2002GL015273.

Hamme, R. C., and S. R. Emerson (2004a), Measurement of dissolved neon by isotope dilution using a quadrupole mass spectrometer, *Mar. Chem.*, *91*(1–4), 53–64, doi:10.1016/j.marchem.2004.05.001.

Hamme, R. C., and S. R. Emerson (2004b), The solubility of neon, nitrogen and argon in distilled water and seawater, *Deep Sea Res. Part I*, *51*(11), 1517–1528, doi:10.1016/j.dsr.2004.06.009.

Hamme, R. C., and S. R. Emerson (2006), Constraining bubble dynamics and mixing with dissolved gases: Implications for productivity measurements by oxygen mass balance, *J. Mar. Res.*, *64*(1), 73–95, doi:10.1357/002224006776412322.

Hamme, R. C., and J. P. Severinghaus (2007), Trace gas disequilibria during deep-water formation, *Deep Sea Res. Part I*, *54*(6), 939–950, doi:10.1016/j.dsr.2007.03.008.

Hohmann, R., P. Schlosser, S. Jacobs, A. Ludin, and R. Weppernig (2002), Excess helium and neon in the southeast Pacific: Tracers for glacial meltwater, *J. Geophys. Res.*, *107*(C11), 3198, doi:10.1029/2000JC000378.

Ito, T., and C. Deutsch (2006), Understanding the saturation state of argon in the thermocline: The role of air-sea gas exchange and diapycnal mixing, *Global Biogeochem. Cycles*, *20*, GB3019, doi:10.1029/2005GB002655.

Ito, T., and M. J. Follows (2005), Preformed phosphate, soft tissue pump and atmospheric CO₂, *J. Mar. Res.*, *63*(4), 813–839, doi:10.1357/0022240054663231.

Jähne, B., G. Heinz, and W. Dietrich (1987a), Measurement of the diffusion coefficients of sparingly soluble gases in water, *J. Geophys. Res.*, *92*(C10), 10,767–10,776, doi:10.1029/JC092iC10p10767.

Jähne, B., K. Münnich, R. Dutzi, W. Huber, and P. Libner (1987b), On the parameters influencing air-water gas exchange, *J. Geophys. Res.*, *92*(C2), 1937–1950, doi:10.1029/JC092iC02p01937.

Knox, F., and M. McElroy (1984), Changes in atmospheric CO₂-Influence of the marine biota at high latitude, *J. Geophys. Res.*, *89*(D3), 4629–4637.

Knox, M., P. D. Quay, and D. Wilbur (1992), Kinetic isotopic fractionation during air-water gas transfer of O₂, N₂, CH₄, and H₂, *J. Geophys. Res.*, *97*(C12), 20,335–20,343.

Ledwell, J. J. (1984), The variation of the gas transfer coefficient with molecular diffusivity, in *Gas Transfer at Water Surfaces*, edited by W. Brutsaert and G. H. Jirka, pp. 293–302, D. Reidel, Hingham, Mass.

Levitus, S. (1982), *Climatological Atlas of the World Ocean*, U.S. Dep. of Commer., NOAA, Rockville, Md.

Luthi, D., et al. (2008), High-resolution carbon dioxide concentration record 650,000–800,000 years before present, *Nature*, *453*, 379–382, doi:10.1038/nature06949.

Marinov, I., A. Gnanadesikan, J. R. Toggweiler, and J. L. Sarmiento (2006), The Southern Ocean biogeochemical divide, *Nature*, *441*, 964–967, doi:10.1038/nature04883.

Martin, J. H., R. M. Gordon, and S. E. Fitzwater (1990), Iron in Antarctic waters, *Nature*, *345*, 156–158, doi:10.1038/345156a0.

Nightingale, P. D., G. Malin, C. S. Law, A. J. Watson, P. S. Liss, M. I. Liddicoat, J. Boutin, and R. C. Upstill-Goddard (2000), In situ evaluation of air-sea gas exchange parameterizations using novel conservative and volatile tracers, *Global Biogeochem. Cycles*, *14*(1), 373–387, doi:10.1029/1999GB900091.

Petit, J. R., J. Jouzel, D. Raynaud, N. I. Barkov, J. M. Barnola, I. Basile, M. Bender, J. Chappellaz, M. Davis, and G. Delaygue (1999), Climate and atmospheric history of the past 420,000 years from the Vostok ice core, Antarctica, *Nature*, *399*, 429–436, doi:10.1038/20859.

Rodehacke, C. B., H. H. Hellmer, O. Huhn, and A. Beckmann (2007), Ocean/ice shelf interaction in the southern Weddell Sea: Results of a regional numerical helium/neon simulation, *Ocean Dyn.*, *57*(1), 1–11, doi:10.1007/s10236-006-0073-2.

Sarmiento, J. L., and J. R. Toggweiler (1984), A new model for the role of the oceans in determining atmospheric *P*CO₂, *Nature*, *308*, 621–624, doi:10.1038/308621a0.

Severinghaus, J. P., A. Grachev, B. Luz, and N. Caillon (2003), A method for precise measurement of argon 40/36 and krypton/argon ratios in trapped air in polar ice with applications to past firn thickness and abrupt climate change in Greenland and at Siple Dome, Antarctica, *Geochim. Cosmochim. Acta*, *67*(3), 325–343, doi:10.1016/S0016-7037(02)00965-1.

Siegenthaler, U., and T. Wenk (1984), Rapid atmospheric CO₂ variations and ocean circulation, *Nature*, *308*, 624–626, doi:10.1038/308624a0.

Sigman, D. M., and E. A. Boyle (2000), Glacial/interglacial variations in atmospheric carbon dioxide, *Nature*, *407*, 859–869.

Sigman, D. M., S. L. Jaccard, and G. H. Haug (2004), Polar ocean stratification in a cold climate, *Nature*, *428*, 59–63, doi:10.1038/nature02357.

Stanley, R. H. R., W. J. Jenkins, and S. C. Doney (2006), Quantifying seasonal air-sea gas exchange processes using noble gas time-series: A design experiment, *J. Mar. Res.*, *64*(2), 267–295, doi:10.1357/002224006777606452.

Stanley, R. H. R., W. J. Jenkins, D. E. Lott, and S. C. Doney (2009), Noble gas constraints on air-sea gas exchange and bubble fluxes., *J. Geophys. Res.*, *114*, C11020, doi:10.1029/2009JC005396.

Stephens, B. B., and R. F. Keeling (2000), The influence of Antarctic sea ice on glacial-interglacial CO₂ variations, *Nature*, *404*, 171–174.

Toggweiler, J. R. (1999), Variation of atmospheric CO₂ by ventilation of the ocean's deepest water, *Paleoceanography*, *14*(5), 571–588, doi:10.1029/1999PA900033.

Toggweiler, J. R., A. Gnanadesikan, S. Carson, R. Murnane, and J. L. Sarmiento (2003a), Representation of the carbon cycle in box models and GCMs: 1. Solubility pump, *Global Biogeochem. Cycles*, *17*(1), 1026, doi:10.1029/2001GB001401.

Toggweiler, J. R., R. Murnane, S. Carson, A. Gnanadesikan, and J. L. Sarmiento (2003b), Representation of the carbon cycle in box models and GCMs: 2. Organic pump, *Global Biogeochem. Cycles*, *17*(1), 1027, doi:10.1029/2001GB001841.

Wanninkhof, R. (1992), Relationship between gas exchange and wind speed over the ocean, *J. Geophys. Res.*, *97*(C5), 7373–7381, doi:10.1029/92JC00188.

Watson, A. J., R. C. Upstill-Goddard, and P. S. Liss (1991), Air-sea gas exchange in rough and stormy seas measured by a dual-tracer technique, *Nature*, *349*, 145–147, doi:10.1038/349145a0.

Weiss, R. F. (1974), Carbon dioxide in water and seawater: The solubility of a non-ideal gas, *Mar. Chem.*, *2*(3), 203–215, doi:10.1016/0304-4203(74)90015-2.

Weiss, R. F., and T. K. Kyser (1978), Solubility of krypton in water and sea water, *J. Chem. Eng. Data*, *23*(1), 69–72, doi:10.1021/je60076a014.

Well, R., and W. Roether (2003), Neon distribution in South Atlantic and South Pacific waters, *Deep Sea Res. Part I*, *50*(6), 721–735, doi:10.1016/S0967-0637(03)00058-X.

Zeebe, R. E., and D. A. Wolf-Gladrow (2001), *CO$_2$ in Seawater: Equilibrium*, *Kinetics*, *Isotopes*, Elsevier Sci., New York.

N. Caillon and J. Jouzel, Laboratoire des Sciences du Climat et de l'Environnement, IPSL, CEA, CNRS, UVSQ, CE Saclay, Orme des Merisiers, F-91191 Gif-sur Yvette, France.

S. Emerson, School of Oceanography, University of Washington, Box 357940, Seattle, WA 98195-7940, USA.

R. C. Hamme, School of Earth and Ocean Sciences, University of Victoria, Bob Wright Centre A405, PO Box 3065 STN CSC, Victoria, BC V8W 3V6, Canada.

D. Nicholson, Department of Marine Chemistry and Geochemistry, Woods Hole Oceanographic Institution, MS 25, 266 Woods Hole Rd., Woods Hole, MA 02543, USA. (dnicholson@whoi.edu)